Multistage hematopoietic stem cell regulation in the mouse: A combined biological and mathematical approach

Celine Bonnet, Panhong Gou, Simon Girel, Vincent Bansaye, Catherine Lacout, Karine Bailly, Marie-Hélène Schlagetter, Evelyne Lauret, Sylvie Méléard, Stéphane Giraudier

iScience

CellPress
OPEN ACCESS

Article

Multistage hematopoietic stem cell regulation in the mouse: A combined biological and mathematical approach

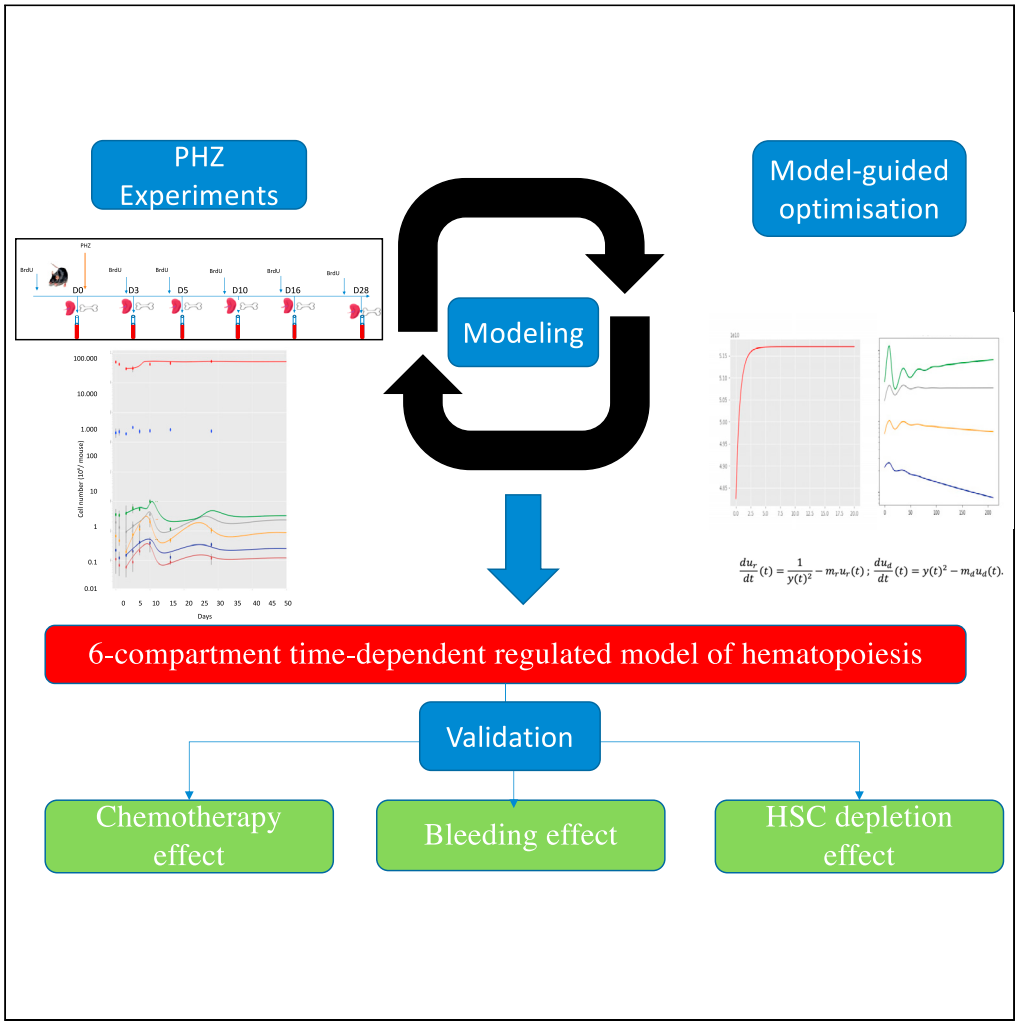

Céline Bonnet, Panhong Gou, Simon Girel, ..., Evelyne Lauret, Sylvie Méléard, Stéphane Giraudier

stephane.giraudier@aphp.fr

Highlights

We describe a new 6-compartment time-dependent regulated model of hematopoiesis

Biological data under steady state and stress and cell dynamics were used

Modeling is able to recapitulate effects from chemotherapy, bleeding, or HSC depletion

Bonnet et al., iScience 24, 103399
December 17, 2021 © 2021
https://doi.org/10.1016/j.isci.2021.103399

iScience

CellPress
OPEN ACCESS

Article

Multistage hematopoietic stem cell regulation in the mouse: A combined biological and mathematical approach

Céline Bonnet,[3,5] Panhong Gou,[1,5] Simon Girel,[3] Vincent Bansaye,[3] Catherine Lacout,[1] Karine Bailly,[2] Marie-Hélène Schlagetter,[1] Evelyne Lauret,[2,6] Sylvie Méléard,[3,4,6] and Stéphane Giraudier[1,6,7,*]

SUMMARY

We have reconciled steady-state and stress hematopoiesis in a single mathematical model based on murine *in vivo* experiments and with a focus on hematopoietic stem and progenitor cells. A phenylhydrazine stress was first applied to mice. A reduced cell number in each progenitor compartment was evidenced during the next 7 days through a drastic level of differentiation without proliferation, followed by a huge proliferative response in all compartments including long-term hematopoietic stem cells, before a return to normal levels. Data analysis led to the addition to the 6-compartment model, of time-dependent regulation that depended indirectly on the compartment sizes. The resulting model was finely calibrated using a stochastic optimization algorithm and could reproduce biological data *in silico* when applied to different stress conditions (bleeding, chemotherapy, HSC depletion). In conclusion, our multi-step and time-dependent model of immature hematopoiesis provides new avenues to a better understanding of both normal and pathological hematopoiesis.

INTRODUCTION

Hematopoiesis provides the lifelong supply of mature blood cells derived from a rare population of bone marrow (BM) multipotent hematopoietic stem cells (HSCs) (Orkin and Zon, 2008; Till and McCulloch, 1961). The lineage relationship between HSCs and the mature blood cells was first proposed as a multistep process in which generations of diverse blood cells are coupled with movement through consecutive hematopoietic stem and progenitor cell (HSPC) compartments. HSPC division and differentiation are controlled by extracellular signals and by intracellular networks. In the classical model, successive HSPC compartments along hematopoietic differentiation processes are defined at an immunophenotypic level, typically by the expression of cell surface marker combinations (Eich et al., 2019; Notta et al., 2016). In this context, since the 1960s, HSCs have typically been functionally defined by their ability to sustain multi-lineage engraftment for an extended period of time upon serial transplantation into irradiated recipient mice (Till and McCulloch, 1961). Recently, however, a new generation of experimental tools allowing *in situ* analysis of HSC output has challenged the classical model by pointing out fundamental differences between physiological unperturbed and stress hematopoiesis (Busch et al., 2015; Carrelha et al., 2018; Chapple et al., 2018; Pei et al., 2017, 2020; Rodriguez-Fraticelli et al., 2018; Säwen et al., 2018; Sun et al., 2014). In native hematopoiesis in particular, progenitors directly downstream of long-term hematopoietic stem cells (LT-HSCs) such as short-term hematopoietic stem cells (ST-HSCs) and multipotent Progenitors (MPPs), serve as a major and nearly self-renewing source of cells for day-to-day hematopoiesis. This renders the blood and immune system less dependent on LT-HSCs, which is consistent with the quiescence of adult LT-HSCs (Busch and Rodewald, 2016; Busch et al., 2015; Foudi et al., 2009; Schoedel et al., 2016; Wilson et al., 2008). In addition, recent single-cell profiling analysis has unveiled the tremendous heterogeneity of each previously defined compartment leading to a continuum in the hematopoiesis process (Giladi et al., 2018; Laurenti and Göttgens, 2018; Paul et al., 2015; Velten et al., 2017). However, punctuated transitions across this continuous gene expression landscape may still exist and represent functionally distinct groups of cells (Liggett and Sankaran, 2020).

Mathematical modeling that integrates both unperturbed and stress hematopoiesis is a powerful approach to addressing key questions in hematopoiesis and can provide both qualitative and quantitative insights

[1]Centre Hayem, Université de Paris, Hôpital Saint Louis, INSERM U1131, 1 Avenue Claude Vellefaux, 75010 Paris, France

[2]Université de Paris, Institut Cochin, INSERM U1016, CNRS UMR8104, 75014 Paris, France

[3]CMAP, CNRS, Ecole Polytechnique, Institut Polytechnique de Paris, 91128 Palaiseau, France

[4]Institut Universitaire de France, Paris, France

[5]These authors contributed equally

[6]Senior author

[7]Lead contact

*Correspondence: stephane.giraudier@aphp.fr

https://doi.org/10.1016/j.isci.2021.103399

into stem cell dynamics and fate commitment. Previous mathematical models based on *in vivo* analyses of immature compartments have been previously reported. They have mostly described immature hematopoiesis dynamics in a steady state. Notably also, these studies have relied upon parameters such as cell division rates or probabilities of self-renewal (Busch et al., 2015; Foudi et al., 2009; Mackey, 2001; Sawai et al., 2016; Wilson et al., 2008). Among these reports, Rodewald and colleagues described a major breakthrough by modeling hematopoiesis based on stem compartments from LT-HSCs to MPPs in unperturbed hematopoiesis (Busch et al., 2015). Nevertheless, these researchers noticed that their steady state model could not fully recapitulate stress hematopoiesis such as 5-fluorouracil (5-FU) treatment, suggesting that unperturbed and stress hematopoiesis do not follow the same biological rules.

Stress hematopoiesis has been also modeled but the *in vivo* data used for this purpose have often focused only on mature cells and not on immature compartments (Angulo et al., 2018; Crauste et al., 2008, 2010; Fuertinger et al., 2013; Klose et al., 2019; Knauer et al., 2020; Loeffler et al., 1989; Mahadik et al., 2019; Manesso et al., 2013; Marciniak-Czochra et al., 2009; Mon Père et al., 2021; Østby et al., 2003, 2004; Rogg et al., 2019; Rubinow and Lebowitz, 1975; Stiehl et al., 2018). In our present study, we have recapitulated steady-state and stress hematopoiesis in a single mathematical model based on *in vivo* experimental data and focusing on HSC and progenitor compartments. We focused in particular on the erythroid responses since these cells represent ~95% of the total blood cells. As the stress condition, we first chose *in vivo* "peripheral stress" through hemolytic anemia (phenylhydrazine [PHZ] administration known to destroy mature red blood cells [RBCs]) to avoid direct alterations of the stem cell compartments (Hara and Ogawa, 1976; Klinken et al., 1987). Most studies to date related to PHZ administration have focused on committed progenitors, whereas we targeted immature compartments in our current analysis.

We demonstrate from our present data that several stress conditions and unperturbed hematopoiesis can be combined into a single system based on a six-immature compartment model. We integrated time-dependent regulations that depended indirectly on compartment sizes. Self-renewal and differentiation dynamics were modulated through two regulators. The model was finely calibrated using a stochastic optimization algorithm (Covariance Matrix Adaptation in Evolution Strategy, CMA-ES) (Hansen and Ostermeier, 2001) based on our experimental observations. Its robustness was assessed numerically, and it was finally validated using various *in silico* stresses such as bleeding, chemotherapy (5-FU administration) or destruction of the most immature LT-HSC compartment as it successfully reproduced biological data *in silico* that had previously been reported in the literature.

RESULTS

General form of a novel regulated compartmental mathematical model

See also STAR Methods, method details.

We developed a mathematical model that could recapitulate both steady-state and stress hematopoiesis from LT-HSC to RBC production. Modeling the kinetics of proliferation/differentiation processes requires a theoretical number of compartments between LT-HSCs and RBCs. We focused on the behavior of the immature LT-HSC, ST-HSC, MPP, common myeloid progenitor (CMP), and megakaryocytic-erythroid progenitor (MEP) cell compartments and that of mature RBCs. Hence, we considered a system of six equations to describe the dynamics on these compartment sizes, comparable with the dynamics introduced previously by Mon Père and colleagues (2021). An additional and formal explanation for the 6-compartment model was developed (STAR Methods, explanation of 6 compartments choice) based on an optimal argument that explains the data under homeostatic conditions, as previously described (Dingli et al., 2007).

Our model describes a hierarchy of 6-cell compartments evolving over time. In brief, a cell of a given compartment can self-renew or differentiate independently from the others and is characterized by its self-renewal and differentiation rates (and for the last compartment corresponding to RBCs, its death rate). Each division is considered symmetric (it was not possible, based on our data, to distinguish symmetrical and asymmetrical divisions). The HSPC death rate (apoptosis) was low (Domen et al., 2000 and our data) and then neglected in our model.

The entire dynamics can be summarized as follows:

Table 1. Determination of the cell number in each compartment per mouse and the percentage of BrdU-positive cells in steady-state hematopoiesis

Cell type	n (10^6/mouse)	BrdU (%)
LT-HSC	0.011 ± 0.070	1.0 ± 2.71
ST-HSC	0.022 ± 0.013	1.4 ± 0.75
MPP	0.067 ± 0.045	6.32 ± 3.58
CMP	0.196 ± 0.111	12.42 ± 2.31
MEP	0.359 ± 0.189	31.75 ± 1.15
GMP	0.677 ± 0.430	19.50 ± 7.50

Data represent the mean values from of at least six mice

$$\frac{dx_1}{dt}(t) = (r_1(t) - d_1(t))x_1(t)$$
$$\frac{dx_i}{dt}(t) = 2d_{i-1}(t)x_{i-1}(t) + (r_i(t) - d_i(t))x_i(t), \quad \text{for } i \in \{2, \ldots 5\},$$
$$\frac{dx_6}{dt}(t) = 2^{n(t)}d_5(t)x_5(t) + d_6x_6(t).$$

For any i = 1, …,4, a cell belonging to the i compartment self-renews at time t at rate R_i (t) > 0 or differentiates to a non-erythroid lineage at rate μ_i or to an erythroid lineage giving rise to two cells in compartment i+1 at rate d_i(t) > 0 (erythroid differentiation). The net proliferation rate is given by r_i (t) = R_i (t) - μ_i. A 5-type cell "differentiates" at rate d_5(t) > 0 and gives rise to $2^{n(t)}$ 6-type cells. These dynamics summarize the n(t) mitosis observed at the end of erythroid differentiation (between MEPs and RBCs). This amplification could be simplified as $2^{n(t)}$ RBC issued from 1 MEP since terminal erythroid differentiation has been largely modeled before and was not our concern. A 6-type cell corresponds to a mature RBC that is dying at the constant rate d_6 > 0.

Parameter calibration of the mathematical model under homeostatic conditions

See also STAR Methods, method details.

Our model system was first calibrated under homeostatic conditions. We evaluated the compartment cell numbers *in vivo* and the proliferation rates at a steady state using BrdU analysis (Table 1). The cell compartment sizes are denoted by x_i*, i = 1, …,6. In the steady state, the net proliferation and differentiation rates are the positive constant values r_i* and d_i*, i = 1, …, 5. Furthermore, presuming that the LT-HSC compartment is at equilibrium, the LT-HSC net proliferation, r_1*, is equal to the differentiation LT-HSC rate, d_1*. Moreover, for any i, ∈ {2,., 5}: d_i*-r_i*>0 to ensure the stability of the system (STAR Methods, explanation for the 6-compartments choice). The lifespan of mature RBCs was based on that reported in the literature: d_6 = 1/40 (/day).

We estimated the values of d_i* and later of r_i* from our BrdU experiments (BrdU being injected 20 h prior to the analysis) and from the erythro-myeloid commitment rates values μ_i (based on Busch et al., 2015; STAR Methods, calibration of the parameters). The BrdU-labeled cell proportion was estimated by:

$$p_i^{BrdU} = \frac{x_i^D(20h)}{x_i^*}$$

where $x_i^D(20h)$ is the number of cells having made a division at least once in a time interval of 20 h. The dynamics of x_i^D is given by the following equation system:

$$\frac{dx_1^D}{dt}(t) = r_1^*x_1^D(t) + 2\left(r_1^* + \mu_1\right)\left(x_1^* - x_1^D(t)\right) - d_1^*x_1^D(t),$$
$$\frac{dx_i^D}{dt}(t) = r_i^*x_i^D(t) + 2\left(r_i^* + \mu_i\right)\left(x_i^* - x_i^D(t)\right) + 2d_{i-1}^*x_{i-1}^* - d_i^*x_i^D(t), \quad \text{for } i \in \{2, \ldots 5\}.$$

This led us to estimate the differentiation and net proliferation rate values at equilibrium as follows:

Table 2. Determination of the net proliferation and differentiation rates, number of the last mitosis, and size of each compartment in the steady state

	Type 1 LT-HSC	Type 2 ST-HSC	Type 3 MPP	Type 4 CMP	Type 5 MEP	Type 6 RBC
Net proliferation rate (/day)	$r^*_1 = 0.006$	$r^*_2 = 0.004$	$r^*_3 = 0.014$	$r^*_4 = 0.032$	$r^*_5 = 0.2$	
Differentiation rate (/day)	$d^*_1 = 0.006$	$d^*_2 = 0.01$	$d^*_3 = 0.02$	$d^*_4 = 0.046$	$d^*_5 = 0.254$	
Size of the compartment (10^6cell/mouse)	$x^*_1 = 0.011$	$x^*_2 = 0.022$	$x^*_3 = 0.067$	$x^*_4 = 0.196$	$x^*_5 = 0.359$	$x^*_6 = 5.17 \times 10^4$
RBC death rate (/day)						$d^*_6 = 0.25$
Last mitosis number						$n^* = 13.79$
Non-erythroid differentiation rate (/day)	$\mu_1 = 0$	$\mu_2 = 0$	$\mu_3 = 0.022$	$\mu_4 = 0.04$	$\mu_5 = 0$	

$$r_1^* = d_1^* = -\frac{24}{40}\log\left(1 - p_1^{BrdU}\right) - \mu_1,$$

$$r_i^* = -\frac{24}{40}\log\left(1 - p_i^{BrdU}\right) - \mu_i - \frac{d_{i-1}^* x_{i-1}^*}{x_i^*}, \quad \text{for } i \in \{2, \ldots 5\},$$

$$d_i^* = r_i^* + \frac{2d_{i-1}^* x_{i-1}^*}{x_i^*}.$$

The n* number of mitoses (between MEPs and RBCs) at equilibrium was deduced by $\log_2\left(\frac{d_6^* x_6^*}{d_5^* x_5^*}\right)$

We then computed all appropriate parameters. We took into consideration the population size (Table 1), net proliferation and differentiation rates, μ_i erythro-myeloid commitment rates (obtained from Busch et al., 2015), and the n* value. These parameters (Table 2) allowed us to characterize unperturbed native hematopoiesis for the normal lifespan of the laboratory mouse.

As a stress condition, we induced an acute hemolytic anemia using PHZ administration (Figure 3A). After a 40% hemolysis level (observed on day 3), a rapid recovery of RBCs was evidenced after 10–16 days (Figure 1A). Our 6-step model was applied to recapitulate this RBC recovery but, as expected, the recovery time exceeded 1 month, which was totally discrepant from the observed biological data (Figure 1A). Indeed, different regulatory processes have to be considered for each compartment's cell dynamics. To determine these factors, biological data were requested.

PHZ treatment impacts immature compartments from LT-HSCs to MEPs *in vivo*

To further elucidate the biological mechanisms responsible for the fast RBC recovery at the level of the HSPC compartments, we analyzed immature compartment modifications after PHZ injections into the blood, BM, and spleen. Briefly, during the first 3 days after injection, we observed a drastic RBC fall, and an increase in platelet and leukocyte counts (Figures 1A–1C), suggesting an inflammatory process associated with hemolytic anemia. Multi-cytokine concentration follow-ups in the blood revealed huge increases in IL-1α, IL-2, IL-6, IL-13, G-CSF, MIP-1α and β, and TNFα at 5 days after PHZ injection (Figure 1D), confirming an inflammatory process. The total number of BM cells was slightly reduced at day 3 (−25%) and enhanced at day 10 (+33%) (Figure 1G). The spleen weight strongly increased 24 h after PHZ injection (Figures 1E and 1F), becoming 3 times larger than normal at day 3, as previously observed after erythroid (Hara and Ogawa, 1976; Sanchez et al., 2006) or social stress in mice (McKim et al., 2018). The three hematopoietic tissues were analyzed to assess the proportion and absolute cell numbers in the different compartments (LT-HSC, ST-HSC, MPP, CMP, and MEP) as well as their proliferation rates (BrdU incorporation), and apoptosis (AnnexinV labeling). In the BM, decreases in all compartment sizes (from LT-HSC to CMP) were evident (Figure 2), whereas the BM MEP population remained relatively stable during this phase. No differences in BrdU incorporation were observed at day 3 in the different BM

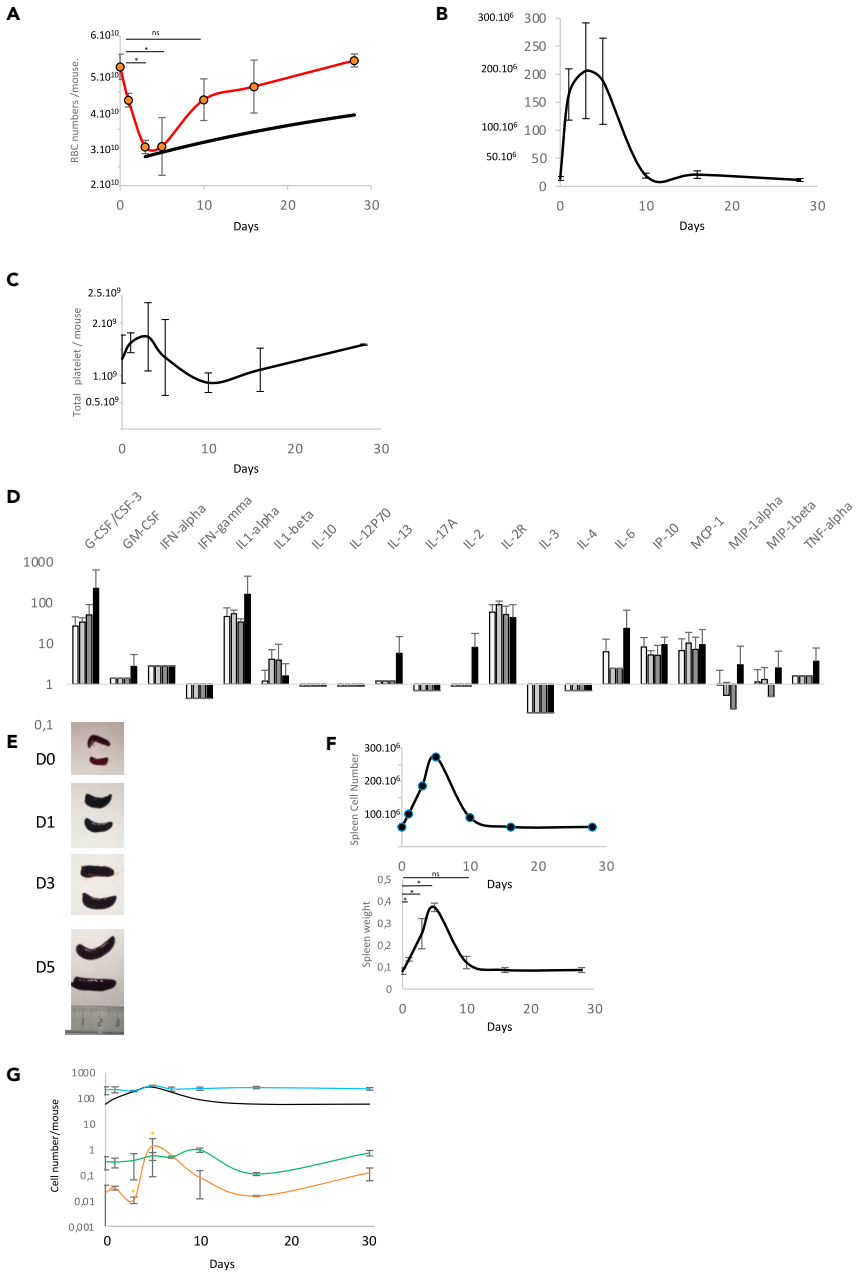

Figure 1. Analysis of blood, spleen, and BM parameters following PHZ-mediated chemical hemolysis

Mice were injected with PHZ (60 mg/kg), and blood, BM, and spleen samples were harvested at the indicated times.

(A) RBC counts (x10^9/mouse) (orange line, biological values; black line, computed values).

(B) White blood cell counts per mouse.

(C) Platelet numbers per mouse.

(D) Cytokine concentrations in the blood at day 0 (white), day 1 (pale gray), day 3 (dark gray), and day 5 (black).

(E) Spleen morphological changes (photographs taken on days 0, 1, 3, and 5).

(F) (Top) Total spleen cell number per mouse (x10^6/mouse). (Bottom) Spleen weight variations.

(G) Follow-up of total cell and MEP numbers for BM and spleen (total BM cells, blue line; total splenic cells, black line; spleen MEPs, green line; BM MEPs, orange line). Values are the mean ± SEM of at least four mice; *$p < 0.05$.

compartments except for MEP, which displayed a 2-fold increased cell proliferation compared with day 0 (Figure 3). In contrast, the number of splenic MEPs, negligible at day 0 compared with the number of BM MEPs (10 times less abundant), displayed a huge increase to reach values comparable with those for

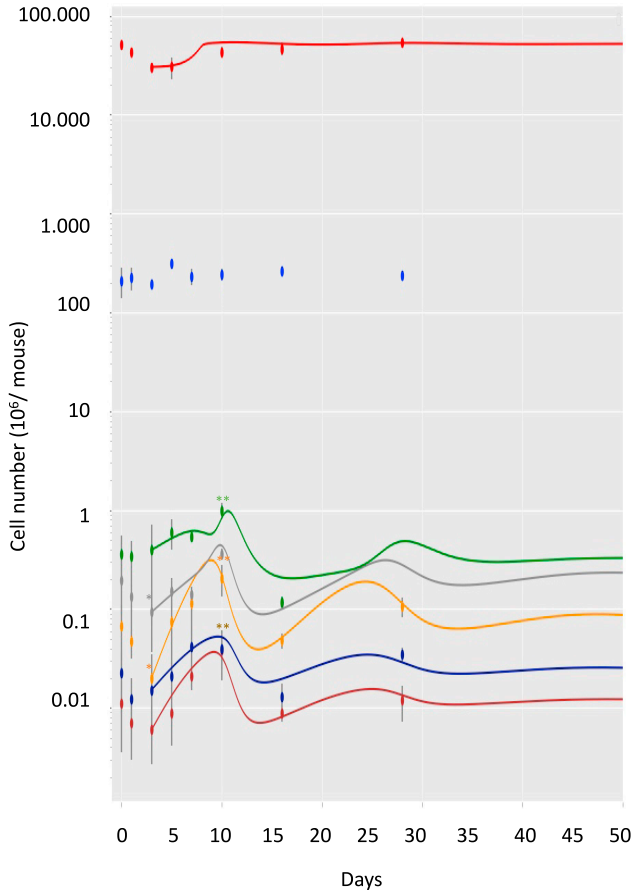

Figure 2. Evolution of experimental and model parameters during PHZ-mediated chemical hemolysis

Red blood cell (RBC) and bone marrow cell numbers per mouse (x10^6/mouse) were assessed from the *in vivo* experiments (red points, RBCs; blue points, total BM cells; green points, BM MEPs; gray points, BM CMPs; orange points, BM MPPs; dark blue points, BM ST-HSCs; brown points, BM LT-HSCs); Mann-Whitney test, **p < 0.05. Values and standard errors were generated from the experimental data for each time point. Evolution curves were deduced from the mathematical modeling.

BM MEPs at 5 days after PHZ injection (Figure 1G). The splenic MEP compartment showed a return to normal values at day 10.

To gain further insights into the mechanisms underlying the drastic decrease in the BM compartment size, we assessed hypothetical mechanisms such as apoptosis, egress from the BM to the blood or to the spleen, or phenotypic changes due to PHZ treatment. No increase in the proportion of AnnexinV-labeled cells was observed for any BM progenitor compartment examined, allowing us to exclude any excess cell death. Blood cell analysis performed at days 3 and 5 after PHZ injection showed a less than 1% proportion of Lin- cells, thus precluding an egress of Lin- or LSK cells from the BM to the blood (Figure S2A). In the spleen, the number of mature cells increased by 3-fold (Figure 1F), whereas the LSK and CMP compartments displayed no significant variations, ruling out any role of splenic immature progenitors on day 3 (data not shown). Lastly, to confirm the functional stemness properties of LT-HSCs exposed to PHZ, competitive BM transplantation with 50% of CD45.1 BM cells from untreated animals and 50% of total BM cells from day 3-PHZ-treated mice was performed in CD45.2-9.5 Gy-irradiated recipients. Blood chimerism analysis 3 months post transplantation showed a decreased proportion of PHZ-treated cells, confirming the decreased number of LT-HSCs in the BM in day 3-PHZ-treated mice (Figure S2C). These data collectively suggest that the decreased BM progenitor compartment sizes (but not involving increased proliferation, apoptosis, or egress to the spleen or blood), and the stable number of MEPs displaying a 2-fold increased proliferation in the BM and spleen, is related to a rapid differentiation process, in order to quickly compensate for the loss of RBCs through a versatile mechanism.

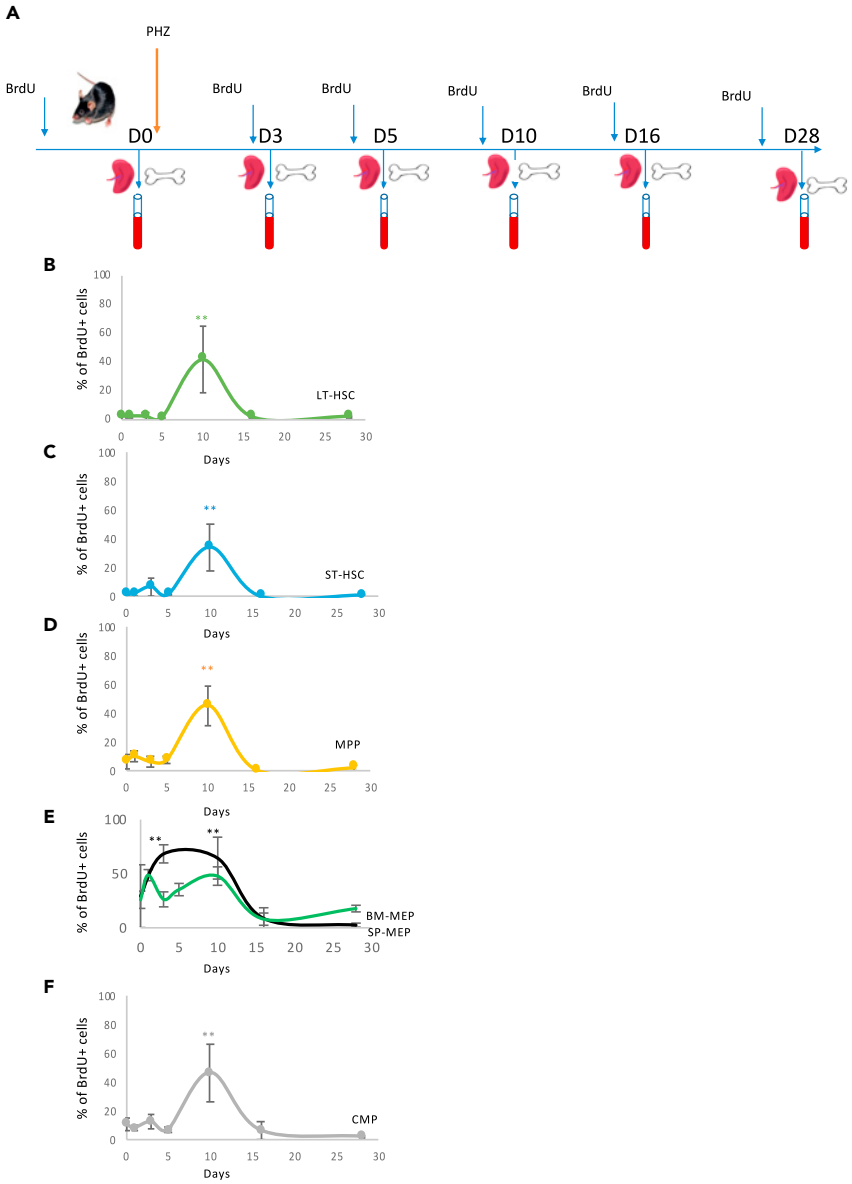

Figure 3. Analysis of BrdU incorporation in HSPCs at different time points after PHZ administration in the mouse

(A) Schematic representation of the PHZ experiments.

(B) BM LT-HSC BrdU+ frequencies 16 h after PHZ administration.

(C) BM ST-HSC BrdU+ frequencies after PHZ administration.

(D) BM MPP BrdU+ frequencies 16 h after PHZ administration.

(E) BM (gray line) and spleen (black line) MEP BrdU+ frequencies 16 h after PHZ administration.

(F) BM CMP BrdU+ frequencies 16 h after PHZ administration. Significance was determined in comparison with D0; Mann-Whitney test $^{**}p < 0.05$ ($n = 5$).

The dynamics of progenitor compartments (determined using the BrdU data and compartment size) during the recovery from the PHZ treatment were analyzed at days 3, 5, 7, 10, 16, and 28 post injection. Recovery was almost effective in all compartments from day 7 to day 10 (Figure 1A). On day 10, all compartments displayed a 2- to 3-fold increase in cell numbers before returning to normal values on day 28. BrdU analysis revealed that all BM compartments exhibited a drastic increase in cell proliferation at day 10 (the hematocrit normalization time point). Thereafter, BrdU incorporation returned to normal values at days 16 and 28 (Figure 3), confirming previous observations (Mackey, 2001).

Adding compartment regulations allows the modeling of steady-state and stress-response hematopoiesis

See also STAR Methods, Method details, Mathematical model.

To model both unperturbed and stress-related hematopoiesis with our dynamical system, we introduced regulatory processes by assuming that previously defined parameters depend indirectly upon the compartment size through dynamics of two regulators (u_r and u_d) that modulate net proliferation and differentiation, thereby exerting positive and negative effects, respectively, on compartment sizes. More precisely, we assumed that $r_i(t)$ and $d_i(t)$ are given by the following equations:

$$r_i(t) = r_i^* \left(25\, m_r\, u_r(t) \right)^{\alpha_i};\quad d_i(t) = d_i^* \left(\frac{m_d}{25}\, u_d(t) \right)^{\beta_i}.$$

r_i^* and d_i^* have been previously defined. α_i and β_i are non-negative real numbers. The two functions u_r and u_d were considered to integrate all of the various biological factors implicated in immature cell compartment dynamics, such as cytokines, chemokines, ROS, and cell-cell interactions (Batsivari et al., 2020). Their dynamics follow a double system of production and clearance described by the following equations:

$$\frac{du_r}{dt}(t) = \frac{1}{y(t)^2} - m_r u_r(t)\ ;\ \frac{du_d}{dt}(t) = y(t)^2 - m_d u_d(t).$$

Production of the regulators is given by functions that depend on BM cell numbers. The y(t) quantity denotes the total number of cells at time t in the five immature compartments, renormalized by their size at equilibrium. The clearance of the regulators after their production is denoted by linear degradation terms described by the m_r and m_d positive parameters. Note that regulatory processes in cellular dynamics are typically considered to be in a quasi-steady state (Knauer et al., 2020; Mon Père et al., 2021; Stiehl et al., 2014). However, such regulation cannot explain the damped oscillations around the equilibrium we observed *in vivo*. However, the two dynamic parameters $u_r(t)$ and $u_d(t)$ in our model allowed us to explain such oscillations by inducing delays between regulator modifications and their effects on compartment sizes. Assuming that the net proliferation rate during late erythropoiesis is regulated in a specific and different manner (erythropoietin, stem cell factor, etc.), RBC production dynamics from MEPs can be considered to be controlled via a different type of regulation. MEP differentiation gives birth to $2^{n(t)}$ RBCs that summarize the n(t) last mitosis with a c-logistic type function of the RBC number as follows:

$$n\left(t\right) = n^* + \left(33 - n^*\right)\left(1 - \left(\frac{x_6(t)}{x_6^*}\right)^c\right).$$

We hypothesized, based on the existing literature (Hayflick, 1965), that the maximum number of mitoses between an MEP and mature RBC was 33, which gave us an upper-bound for n* in our model. The c parameter is a positive number.

Parameter calibration based on experimental data with the CMA-ES algorithm

The parameters in our regulated model were calibrated using a stochastic optimization algorithm based on a CMA-ES method (CMA-ES; Hansen and Ostermeier, 2001), which minimizes discrepancy between simulated and experimental data (STAR Methods, calibration of feedback parameters). The optimal parameters obtained by this method are presented in Table 3, and the corresponding cell dynamics are shown in Figure 1. Sensitivity analysis was also performed (STAR Methods, sensitivity analysis) and matched the experimental data in all compartments after PHZ-induced stress (including the damped oscillation around the equilibrium) as well as in the steady state.

In silico model validation through various hematopoietic stress conditions

To assess the robustness of our model under different stress conditions, we developed three different *in silico* hematopoietic stresses and compared the predictive values obtained using our model with biological data reported in the literature. At first, we assessed a 15% loss of RBCs (comparable with a hemorrhage) as studied previously in the mouse *in vivo* (Raabe et al., 2011). Our model predicted a normalization of the red cell mass within 3–4 days, as expected (Figure 4A). Moreover, no major effect on the most immature compartments was predicted by our model in accordance with previously reported biological data (data not shown). We next modeled the effects of the commonly used 5-FU treatment, a chemotherapeutic compound that can force quiescent LT-HSCs to enter the cell cycle at 4–10 days after injection without perturbation of blood parameters. 5-FU specifically kills cycling cells at 24–48 h post injection, and consistently,

Table 3. Compartment proliferation and erythroid differentiation rate constants, clearance of proliferation and differentiation regulators, and mitotic number in the transition from MEPs to mature RBCs after a stress event

	Type 1 LT-HSC	Type 2 ST-HSC	Type 3 MPP	Type 4 CMP	Type 5 MEP	
Regulation sensitivity parameter for the net proliferation rate	$\alpha_1 = 4.56$	$\alpha_2 = 4.53$	$\alpha_3 = 4.0$	$\alpha_4 = 2.2$	$\alpha_5 = 0.0$	
Regulation sensitivity parameter for the differentiation rate	$\beta_1 = 9.17$	$\beta_2 = 8.95$	$\beta_3 = 8.24$	$\beta_4 = 6.2$	$\beta_5 = 4.9$	
Proliferation regulator clearance (/day)						$m_r = 0.1$
Differentiation regulator clearance (/day)						$m_d = 0.057$
Last mitosis sensitivity parameter						$c = 0.79$

All parameters have been defined in the results section.

our model indicated the drastic and direct death of all proliferating hematopoietic cells for 2 days. We further observed *in silico* that immature compartments entered the cell cycle at 4–10 days after 5-FU treatment without any dramatic effect on mature circulating cells (Figure 4B), consistent with previous report (D'Hondt et al., 2001). Finally, we applied a third type of stress based on a specific eradication of the LT-HSC compartment as reported by Schoedel and co-workers (Schoedel et al., 2016). We found that our *in silico* mouse model maintained mature hematopoiesis and also immature compartment (MEP, CMP) sizes with a reduced number of ST-HSCs as observed in the Schoedel study for the lifespan of the mice (Figure 4C). Taken together, these three aforementioned *in silico* predictions confirmed the robustness of our model.

DISCUSSION

Our present interdisciplinary study marries mathematical modeling and experimental work to provide a mathematical model that can reconcile steady-state and stress hematopoiesis under various stress conditions. We focused on erythropoietic differentiation since this represents more than 90% of all blood cells, thus excluding other differentiation lineages that have previously been modeled quite extensively (Craig et al., 2016; Knauer et al., 2020). We also highlighted a mechanism in our current analyses by which transient stress exposure leads to a protracted influence on all progenitor compartments, including LT-HSCs, resulting in a fast repopulation of mature compartments.

In order to study stress-response hematopoiesis, the PHZ "stress model" was initially considered. PHZ is a chemical compound that can induce hemolysis. Nevertheless, this process also induced a huge inflammatory response leading to changes in all blood cell types and a very large cytokine storm in the few days following PHZ administration. Regardless of the nature of the alterations to hematological parameters (such as anemia or inflammation), we took advantage of the direct *in vivo* modifications of immature compartments to model the normalization of the compartment sizes upon exposure to stress. Our model could faithfully reproduce the return to baseline of the hematopoietic compartments. We next applied it to three other types of "classical" murine stress conditions, such as bleeding, 5-FU chemotherapy, and LT-HSC attrition. The *in silico* predictions in each case accorded with the biological data reported in the literature, further reinforcing the robustness of our model.

The consequences of hematopoietic stress on stem cell compartments such as LT-HSC, ST-HSC, MPP, CMP, and MEP can be drastic. Our present experiments demonstrated that, after an acute stress event that caused massive RBC loss, associated with a cytokine storm, the first compensatory mechanism entails all compartments, from LT-HSC to CMP, and, surprisingly, induces differentiation without proliferation as a first step in this recovery process. The following recovery phase not only replenishes the different "flushed" compartments but exceeds steady-state values. Normalization of all compartment sizes occurs in a third phase similar to dampened oscillations around the standard values. Importantly,

A

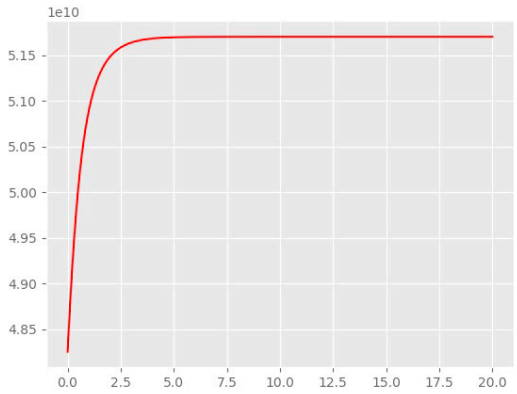

B

	Days 2-3	Days 3-4	Days 4-5	Days 5-6	Days 6-7	Days 10-11	Days 15-16	Days 30-31	Steady-state
LT-HSC BrdU+ (%)	1.7	2.0	2.4	2.7	2.9	2.8	1.8	1.0	1.0
ST-HSC BrdU+ (%)	1.6	1.7	1.9	2.0	2.1	2.0	1.5	1.5	1.4
MPP BrdU+ (%)	8.4	8.9	9.4	9.8	10.0	9.9	8.0	7.4	6.3
CMP BrdU+ (%)	15.6	16.0	16.5	16.7	16.9	16.8	15.0	15.6	12.4
MEP BrdU+ (%)	38.0	37.0	36.8	36.4	36.0	35.0	35.5	38.8	31.8

C

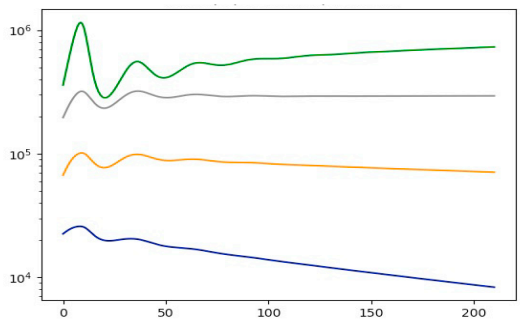

Figure 4. Application of the novel mathematical model to three different stress conditions

(A) Bleeding: Red line: modeled blood RBC number recovery after 15% loss of RBC

(B) 5-FU administration: Theoretical percentage of BrdU+ cells after 5-FU administration.

(C) LT-HSC depletion. Time evolution of ST-HSC (blue line), MPP (orange line), CMP (gray line), and MEP cells (green line) after theoretical LT-HSC destruction.

these cell number oscillations targeting each compartment revealed by our model accord with the *in vivo* data previously reported for post-chemotherapy stressed hematopoiesis (Busch et al., 2015). In contrast to the above responses, the MEP compartment was found not to be subjected to such a strong regulatory step in the BM, probably because of the well-known spleen stress erythropoiesis process that is mediated by a different kind of regulation, as documented here and in previous reports (Perry et al., 2009).

Our current study focused on immature cell compartments unlike most prior studies that have focused on late erythropoiesis. We considered late erythropoiesis to be one single compartment regulated by specific factors (such as erythropoietin [EPO] and stem cell factor) that are capable of modulating the mitotic

number between MEPs and RBCs. Conversely, immature compartments are regulated by numerous factors. Cytokines/chemokines (e.g., IFNs, TNF, TGFβ, BMP), interactions with niche cells, and neuronal influxes play major roles in the regulation of stem cell compartments (Baldridge et al., 2011; Batsivari et al., 2020; Matatall et al., 2016; Renders et al., 2021). Although biological processes regulating stem compartments in the BM niche seem to be very complex, a surprising finding was that a "proliferation" and a "differentiation" regulator were sufficient to integrate this complexity.

Modeling of the regulation of immature compartments (based on human data) using a mathematical approach similar to ours was recently reported (Mon Père et al., 2021). However, that prior human modeling approach focused on erythroid mature stress conditions related to the loss of mature cells (due to blood loss) or chronic hemolysis (paroxysmal hemolytic anemia). By contrast, we validated our current model using a larger spectrum of stress events targeting not only erythroid mature compartments but also more immature ones via inflammation and acute hemolysis, the destruction of proliferative cells, or LT-HSCs.

Our post-stress experimental data revealed dampened oscillations that were not explained when considering the regulators in a quasi-steady state. We then considered their production/clearance dynamics, which implicitly created a delay in the dampening phenomenon and better matching to our data. Many models to date have included the regulation of the more immature HSC compartments following a brief stress exposure and are based on *in vitro* cell counts (Mahadik et al., 2019), *in vivo* immature (Klose et al., 2019) or mature (Marciniak-Czochra et al., 2009) cell counts, or *in vivo* recovery times (Manesso et al., 2013). To our knowledge, none of these systems displayed the dampening of oscillations within stem cell compartments that we observed previously *in vivo* (we do not consider this to include sustained periodic oscillations that can emerge in chronic infections) (Knauer et al., 2020) Similar oscillations within the late progenitor compartment following EPO administration (Schirm et al., 2013) or RBC suppression (Crauste et al., 2008, 2010; Wulff et al., 1989) have been exhibited by several prior models. However, as the so-called late progenitors in those studies are downstream of the MEP compartment, their proliferation rate is regulated by an EPO-dependent mechanism in contrast to the immature stem cell compartments that we focused on here.

In conclusion, we have successfully modeled the plasticity of hematopoiesis that recapitulates steady-state as well as stress hematopoiesis impacting all immature compartments. Our mathematical model integrates, as finely as possible, the reactions to the principal stress events in immature and RBC compartments and may thus be used to forecast stem cell compartment behaviors *in silico* to the hematopoietic toxicity of drugs such as chemotherapeutics or environmental toxins when the mechanisms of action of these agents are known. Our model also opens avenues to the analysis of malignant clonal development and invasion, noting that stem cell disorders, just like leukemias and cancers in general, could arise from successive stress events if pathological clonal cells react differently from normal cells in response to these conditions.

Limitations of the study

The biological limitations of our present study mainly arise from the use of mouse models in the place of human data. This is a particularly important consideration as hematopoietic stress involves a splenic response in the mouse but not in humans. Another notable limitation was our use of BrdU to analyze the proliferation of immature compartments as this type of analysis has been extensively criticized for its lack of precision. The mathematical limitations of our study include a simplified regulation of the erythroid terminal maturation process (from MEPs to RBCs) that has been extensively described and modeled previously. Modeling of the dynamics between these cell types is summarized by the instant production of 2^n RBCs from MEPs in our model. A second mathematical limitation of note was our reduction of the complex stem cell dynamics to two simple regulators. This reduction was related to the system complexity. However, identifying real and measurable regulators that target these compartments has thus far proved to be very difficult through current biological approaches.

STAR★METHODS

Detailed methods are provided in the online version of this paper and include the following:

- KEY RESOURCES TABLE
- RESOURCE AVAILABILITY
  - Lead contact

SUPPLEMENTAL INFORMATION

Supplemental information can be found online at https://doi.org/10.1016/j.isci.2021.103399.

ACKNOWLEDGMENTS

The authors are grateful to Christine Chomienne (MD/PhD, INSERM U1131) for helpful discussions and assistance with editing the manuscript. The authors greatly acknowledge the Cochin Cytometry and Immunobiology Facility and the IRSL Animal Facility, Université de Paris and also the support from Plan Cancer 2014-2019 (Mathematical Modeling of Myeloproliferative Neoplasms, M^3PN). Supported by grants from the INSERM and INCa 2018 and fellowships from The Research Ministry of China.

AUTHOR CONTRIBUTIONS

C.B., S. Girel, V.B., and S.M. conducted the mathematical modeling. P.G., C.L., K.B., M.-H.S., E.L., and S. Giraudier conducted the *in vivo* experiments. E.L. and S.Giraudier. performed the data analysis. C.B., S. Girel, E.L., S.M., and S. Giraudier wrote the paper.

DECLARATION OF INTERESTS

The authors declare no competing financial or other interests in relation to this study.

Received: January 15, 2021
Revised: July 29, 2021
Accepted: November 2, 2021
Published: December 17, 2021

REFERENCES

Angulo, O., Gandrillon, O., and Crauste, F. (2018). Investigating the role of the experimental protocol in phenylhydrazine-induced anemia on mice recovery. J. Theor. Biol. *437*, 286–298.

Baldridge, M.T., King, K.Y., and Goodell, M.A. (2011). Inflammatory signals regulate hematopoietic stem cells. Trends Immunol. *32*, 57–65.

Batsivari, A., Haltalli, M.L.R., Passaro, D., Pospori, C., Lo Celso, C., and Bonnet, D. (2020). Dynamic responses of the haematopoietic stem cell niche to diverse stresses. Nat. Cell Biol. *22*, 7–17.

Boggs, D.R. (1984). The total marrow mass of the mouse: A simplified method of measurement. Am. J. Hematol. *16*, 277–286.

Busch, K., and Rodewald, H.-R. (2016). Unperturbed vs. post-transplantation hematopoiesis: Both in vivo but different. Curr. Opin. Hematol. *23*, 295–303.

Busch, K., Klapproth, K., Barile, M., Flossdorf, M., Holland-Letz, T., Schlenner, S.M., Reth, M., Höfer, T., and Rodewald, H.-R. (2015). Fundamental properties of unperturbed haematopoiesis from stem cells in vivo. Nature *518*, 542–546.

Carrelha, J., Meng, Y., Kettyle, L.M., Luis, T.C., Norfo, R., Alcolea, V., Boukarabila, H., Grasso, F., Gambardella, A., Grover, A., et al. (2018). Hierarchically related lineage-restricted fates of multipotent haematopoietic stem cells. Nature *554*, 106–111.

Chapple, R.H., Tseng, Y.-J., Hu, T., Kitano, A., Takeichi, M., Hoegenauer, K.A., and Nakada, D. (2018). Lineage tracing of murine adult hematopoietic stem cells reveals active contribution to steady-state hematopoiesis. Blood Adv. *2*, 1220–1228.

Chervenick, P.A., Boggs, D.R., Marsh, J.C., Cartwright, G.E., and Wintrobe, M.M. (1968). Quantitative studies of blood and bone marrow neutrophils in normal mice. Am. J. Physiol. *215*, 353–360.

Craig, M., Humphries, A.R., and Mackey, M.C. (2016). A mathematical model of granulopoiesis incorporating the negative feedback dynamics and kinetics of G-CSF/neutrophil binding and internalization. Bull. Math. Biol. *78*, 2304–2357.

Crauste, F., Pujo-Menjouet, L., Génieys, S., Molina, C., and Gandrillon, O. (2008). Adding self-renewal in committed erythroid progenitors improves the biological relevance of a mathematical model of erythropoiesis. J. Theor. Biol. *250*, 322–338.

Crauste, F., Demin, I., Gandrillon, O., and Volpert, V. (2010). Mathematical study of feedback control roles and relevance in stress erythropoiesis. J. Theor. Biol. *263*, 303–316.

D'Hondt, L., Carlson, J., Benoit, B., Reilly, J., Grimaldi, C., Wuu, J., Lambert, J.F., Dooner, M.S., and Quesenberry, P.J. (2001). Influence of timing of administration of 5-fluorouracil to donors on bone marrow engraftment in nonmyeloablated hosts. Int. J. Hematol. *74*, 79–85.

Dingli, D., Traulsen, A., and Pacheco, J.M. (2007). Compartmental architecture and dynamics of hematopoiesis. PLoS One *2*, e345.

Domen, J., Cheshier, S.H., and Weissman, I.L. (2000). The role of apoptosis in the regulation of hematopoietic stem cells: Overexpression of Bcl-2 increases both their number and repopulation potential. J. Exp. Med. *191*, 253–264.

Eich, M., Trumpp, A., and Schmitt, S. (2019). OMIP-059: Identification of mouse hematopoietic stem and progenitor cells with simultaneous detection of CD45.1/2 and controllable green fluorescent protein expression by a single staining panel. Cytometry A *95*, 1049–1052.

Foudi, A., Hochedlinger, K., Van Buren, D., Schindler, J.W., Jaenisch, R., Carey, V., and Hock, H. (2009). Defining hematopoietic stem and progenitor cell turnover by analysis of histone 2B-GFP dilution. Nat. Biotechnol. *27*, 84.

Fuertinger, D.H., Kappel, F., Thijssen, S., Levin, N.W., and Kotanko, P. (2013). A model of erythropoiesis in adults with sufficient iron availability. J. Math. Biol. *66*, 1209–1240.

Giladi, A., Paul, F., Herzog, Y., Lubling, Y., Weiner, A., Yofe, I., Jaitin, D., Cabezas-Wallscheid, N., Dress, R., Ginhoux, F., et al. (2018). Single-cell characterization of haematopoietic progenitors and their trajectories in homeostasis and perturbed haematopoiesis. Nat. Cell Biol. *20*, 836–846.

Hansen, N., and Ostermeier, A. (2001). Completely derandomized self-adaptation in evolution strategies. Evol. Comput. *9*, 159–195.

Hara, H., and Ogawa, M. (1976). Erthropoietic precursors in mice with phenylhydrazine-induced anemia. Am. J. Hematol. *1*, 453–458.

Hayflick, L. (1965). The limited in vitro lifetime of human diploid cell strains. Exp. Cell Res. *37*, 614–636.

Klinken, S.P., Holmes, K.L., Fredrickson, T.N., Erner, S.M., and Morse, H.C. (1987). Phenylhydrazine stimulates lymphopoiesis and accelerates Abelson murine leukemia virus-induced pre-B cell lymphomas. J. Immunol. *139*, 3091–3098.

Klose, M., Florian, M.C., Gerbaulet, A., Geiger, H., and Glauche, I. (2019). Hematopoietic stem cell dynamics are regulated by progenitor demand: Lessons from a quantitative modeling approach. Stem Cells *37*, 948–957.

Knauer, F., Stiehl, T., and Marciniak-Czochra, A. (2020). Oscillations in a white blood cell production model with multiple differentiation stages. J. Math. Biol. *80*, 575–600.

Knaupp, W., Khilnani, S., Sherwood, J., Scharf, S., and Steinberg, H. (1985). Erythropoietin response to acute normobaric hypoxia in humans. J. Appl. Physiol. *73*, 837–840.

Laurenti, E., and Göttgens, B. (2018). From haematopoietic stem cells to complex differentiation landscapes. Nature *553*, 418–426.

Li, H., Natarajan, A., Ezike, J., Barrasa, M.I., Le, Y., Feder, Z.A., Yang, H., Ma, C., Markoulaki, S., and Lodish, H.F. (2019). Rate of progression through a continuum of transit-amplifying progenitor cell states regulates blood cell production. Dev. Cell *49*, 118–129.e7.

Liggett, L.A., and Sankaran, V.G. (2020). Unraveling hematopoiesis through the lens of genomics. Cell *182*, 1384–1400.

Loeffler, M., Pantel, K., Wulff, H., and Wichmann, H.E. (1989). A mathematical model of erythropoiesis in mice and rats. Part 1: Structure of the model. Cell Tissue Kinet. *22*, 13–30.

Mackey, M.C. (2001). Cell kinetic status of haematopoietic stem cells. Cell Prolif. *34*, 71–83.

Mahadik, B., Hannon, B., and Harley, B.A.C. (2019). A computational model of feedback-mediated hematopoietic stem cell differentiation in vitro. PLoS One *14*, e0212502.

Mahajan, M.M., Cheng, B., Beyer, A.I., Mulvaney, U.S., Wilkinson, M.B., Fomin, M.E., and Muench, M.O. (2015). A quantitative assessment of the content of hematopoietic stem cells in mouse and human endosteal-bone marrow: A simple and rapid method for the isolation of mouse central bone marrow. BMC Hematol. *15*, 9.

Manesso, E., Teles, J., Bryder, D., and Peterson, C. (2013). Dynamical modelling of haematopoiesis: An integrated view over the system in homeostasis and under perturbation. J. R. Soc. Interface *10*, 20120817.

Marciniak-Czochra, A., Stiehl, T., Ho, A.D., Jäger, W., and Wagner, W. (2009). Modeling of asymmetric cell division in hematopoietic stem cells–regulation of self-renewal is essential for efficient repopulation. Stem Cells Dev *18*, 377–385.

Matatall, K.A., Jeong, M., Chen, S., Sun, D., Chen, F., Mo, Q., Kimmel, M., and King, K.Y. (2016). Chronic infection depletes hematopoietic stem cells through stress-induced terminal differentiation. Cell Rep. *17*, 2584–2595.

McKim, D.B., Yin, W., Wang, Y., Cole, S.W., Godbout, J.P., and Sheridan, J.F. (2018). Social stress mobilizes hematopoietic stem cells to establish persistent splenic myelopoiesis. Cell Rep. *25*, 2552–2562.e3.

Mon Père, N.V., Lenaerts, T., Pacheco, J.M.D.S., and Dingli, D. (2021). Multistage feedback-driven compartmental dynamics of hematopoiesis. iScience *24*, 102326.

Notta, F., Zandi, S., Takayama, N., Dobson, S., Gan, O.I., Wilson, G., Kaufmann, K.B., McLeod, J., Laurenti, E., Dunant, C.F., et al. (2016). Distinct routes of lineage development reshape the human blood hierarchy across ontogeny. Science *351*, aab2116.

Orkin, S.H., and Zon, L.I. (2008). Hematopoiesis: An evolving paradigm for stem cell biology. Cell *132*, 631–644.

Østby, I., Rusten, L.S., Kvalheim, G., and Grøttum, P. (2003). A mathematical model for reconstitution of granulopoiesis after high dose chemotherapy with autologous stem cell transplantation. J. Math. Biol. *47*, 101–136.

Østby, I., Kvalheim, G., Rusten, L.S., and Grøttum, P. (2004). Mathematical modeling of granulocyte reconstitution after high-dose chemotherapy with stem cell support: Effect of post-transplant G-CSF treatment. J. Theor. Biol. *231*, 69–83.

Paul, F., Arkin, Y., Giladi, A., Jaitin, D.A., Kenigsberg, E., Keren-Shaul, H., Winter, D., Lara-Astiaso, D., Gury, M., Weiner, A., et al. (2015). Transcriptional heterogeneity and lineage commitment in myeloid progenitors. Cell *163*, 1663–1677.

Pei, W., Feyerabend, T.B., Rössler, J., Wang, X., Postrach, D., Busch, K., Rode, I., Klapproth, K., Dietlein, N., Quedenau, C., et al. (2017). Polylox barcoding reveals haematopoietic stem cell fates realized in vivo. Nature *548*, 456–460.

Pei, W., Shang, F., Wang, X., Fanti, A.-K., Greco, A., Busch, K., Klapproth, K., Zhang, Q., Quedenau, C., Sauer, S., et al. (2020). Resolving fates and single-cell transcriptomes of hematopoietic stem cell clones by PolyloxExpress barcoding. Cell Stem Cell *27*, 383–395.e8.

Perry, J.M., Harandi, O.F., Porayette, P., Hegde, S., Kannan, A.K., and Paulson, R.F. (2009). Maintenance of the BMP4-dependent stress erythropoiesis pathway in the murine spleen requires hedgehog signaling. Blood *113*, 911–918.

Raabe, B.M., Artwohl, J.E., Purcell, J.E., Lovaglio, J., and Fortman, J.D. (2011). Effects of weekly blood collection in C57BL/6 mice. J. Am. Assoc. Lab Anim. Sci. *50*, 680–685.

Renders, S., Svendsen, A.F., Panten, J., Rama, N., Maryanovich, M., Sommerkamp, P., Ladel, L., Redavid, A.R., Gibert, B., Lazare, S., et al. (2021). Niche derived netrin-1 regulates hematopoietic stem cell dormancy via its receptor neogenin-1. Nat. Commun. *12*, 608.

Rodriguez-Fraticelli, A.E., Wolock, S.L., Weinreb, C.S., Panero, R., Patel, S.H., Jankovic, M., Sun, J., Calogero, R.A., Klein, A.M., and Camargo, F.D. (2018). Clonal analysis of lineage fate in native haematopoiesis. Nature *553*, 212–216.

Rogg, S., Fuertinger, D.H., Volkwein, S., Kappel, F., and Kotanko, P. (2019). Optimal EPO dosing in hemodialysis patients using a non-linear model predictive control approach. J. Math. Biol. *79*, 2281–2313.

Rubinow, S.I., and Lebowitz, J.L. (1975). A mathematical model of neutrophil production and control in normal man. J. Math. Biol. *1*, 187–225.

Sanchez, M., Weissman, I.L., Pallavicini, M., Valeri, M., Guglielmelli, P., Vannucchi, A.M., Migliaccio, G., and Migliaccio, A.R. (2006). Differential amplification of murine bipotent megakaryocytic/erythroid progenitor and precursor cells during recovery from acute and chronic erythroid stress. Stem Cells *24*, 337–348.

Sawai, C.M., Babovic, S., Upadhaya, S., Knapp, D.J.H.F., Lavin, Y., Lau, C.M., Goloborodko, A., Feng, J., Fujisaki, J., Ding, L., et al. (2016). Hematopoietic stem cells are the major source of multilineage hematopoiesis in adult animals. Immunity *45*, 597–609.

Säwen, P., Eldeeb, M., Erlandsson, E., Kristiansen, T.A., Laterza, C., Kokaia, Z., Karlsson, G., Yuan, J., Soneji, S., Mandal, P.K., et al. (2018). Murine HSCs contribute actively to native hematopoiesis but with reduced differentiation capacity upon aging. Elife *7*, e41258.

Schirm, S., Engel, C., Loeffler, M., and Scholz, M. (2013). A biomathematical model of human erythropoiesis under erythropoietin and chemotherapy administration. PLoS One *8*, e65630.

Schoedel, K.B., Morcos, M.N.F., Zerjatke, T., Roeder, I., Grinenko, T., Voehringer, D., Göthert, J.R., Waskow, C., Roers, A., and Gerbaulet, A. (2016). The bulk of the hematopoietic stem cell population is dispensable for murine steady-state and stress hematopoiesis. Blood *128*, 2285–2296.

Stiehl, T., Ho, A.D., and Marciniak-Czochra, A. (2014). Assessing hematopoietic (stem-) cell behavior during regenerative pressure. Adv. Exp. Med. Biol. *844*, 347–367.

Stiehl, T., Ho, A.D., and Marciniak-Czochra, A. (2018). Mathematical modeling of the impact of cytokine response of acute myeloid leukemia cells on patient prognosis. Sci. Rep. *8*, 1–11.

Sun, J., Ramos, A., Chapman, B., Johnnidis, J.B., Le, L., Ho, Y.-J., Klein, A., Hofmann, O., and Camargo, F.D. (2014). Clonal dynamics of native haematopoiesis. Nature *514*, 322–327.

Till, J.E., and McCulloch, E.A. (1961). A direct measurement of the radiation sensitivity of normal mouse bone marrow cells. Radiat. Res. *178*, 3–7.

Velten, L., Haas, S.F., Raffel, S., Blaszkiewicz, S., Islam, S., Hennig, B.P., Hirche, C., Lutz, C., Buss, E.C., Nowak, D., et al. (2017). Human haematopoietic stem cell lineage commitment is a continuous process. Nat. Cell Biol. *19*, 271–281.

Wilson, A., Laurenti, E., Oser, G., van der Wath, R.C., Blanco-Bose, W., Jaworski, M., Offner, S., Dunant, C.F., Eshkind, L., Bockamp, E., et al. (2008). Hematopoietic stem cells reversibly switch from dormancy to self-renewal during homeostasis and repair. Cell *135*, 1118–1129.

Wulff, H., Wichmann, H.E., Pantel, K., and Loeffler, M. (1989). A mathematical model of erythropoiesis in mice and rats. Part 3: Suppressed erythropoiesis. Cell Tissue Kinet. *22*, 51–61.

STAR★METHODS

KEY RESOURCES TABLE

REAGENT or RESOURCE	SOURCE	IDENTIFIER
Antibodies		
Biotin anti-mouse Lin Panel	Biolegend	133307
Ter-119, M1/70, RB6-8C5, 145-2C11, RA3-6B2		
APC/Cy7 Streptavidin	Biolegend	405208
BV 510™ anti-mouse Ly-6A/E (Sca-1-) D7	Biolegend	108129
BV421 anti-mouse CD135 A2F10	Biolegend	135315
BV711 anti-mouse CD48 HM48-1	Biolegend	103439
PE/Cy7 anti-mouse CD150 TC15-12F12.2	Biolegend	115914
BB700 Anti-Mouse CD117 (PerCP) 2B8	BD Pharmingen	566414
BV786 Anti-Mouse CD16/CD32 2.4G2	BD Pharmingen	740851
Alexa Fluor® 647 anti-Mouse CD34 Ram34	BD Pharmingen	560230
Alexa Fluor 488 anti-BrdU Antibody	Biolegend	364105
FITC anti-mouse CD45.1 A20	Biolegend	110705
PE anti mouse CD45.2 104	Biolegend	109808
Chemicals, peptides, and recombinant proteins		
PHZ (Phenylhydrazine)	Sigma-Aldrich	P26252
Critical commercial assays		
Zombie UV fixable viability kit	Ozyme	BLE423107
BD Horizon Brilliant staining buffer	BD Pharmingen	563794
Ultracomp ebeads	Life Technologies	01-2222-42
Rainbow Calibration Particles (8 - PEaks), 3.0-3.4 mm SPHERO Particles	BD Pharmingen	559123
BD Pharmingen BrdU Flow Kit	BD Pharmingen	557892
FITC Annexin V Apoptosis Detection Kit	BD Pharmingen	559763
ACK Lysing Buffer, Quality Biological	VWR	10128-802
ProcartaPlex TM Multiplex Immunoassay	Thermofisher (custom multiplex assay have been designed by the authors)	
Experimental models: Organism/strain		
C57BL/6JJanvier (Le Genest, France)		
B6.SJL-Ptprc^{a}Pepc^{b}/BoyCrl Congenic (Ly5.1 mice) Janvier (Le Genest, France)		
Software and algorithms		
Diva software	Beckman	
Kaluza software	Beckman	
Prism 7	https://www.graphpad.com/scientificsoftware/prism/	
Covariance matrix adaptative in Evolution algorithm (CMAES) Python language		
Others		
Tubes MS EDTA	#3MSR0506 Melet Schoesing Lab	
MS9 coulter	Schloessing Melet, Cergy-Pontoise, France)	

(*Continued on next page*)

Continued

REAGENT or RESOURCE	SOURCE	IDENTIFIER
Bioplex MAGPIX Multiplex Reader	Biorad	
Phosphate buffered saline (PBS)	Life Technologies (14190-144)	
DMEM Dulbecco's modified Eagle Medium	Life Technologies 31966-021	

RESOURCE AVAILABILITY

Lead contact

Further information and requests for resources and reagents should be directed to Professor S. Giraudier (stephane.giraudier@aphp.fr).

Materials availability

All reagents used in this study are commercially available.

Data and code availability

- Data reported in this paper will be shared by the lead contact upon request.
- This paper does not report original code.
- Any additional information required to reanalyze the data reported in this paper is available from the lead contact upon request.

EXPERIMENTAL MODEL AND SUBJECT DETAILS

Mice

Adult 6-12 week old C57BL/6 (CD45.2) and C57BL/6.SJL (CD45.1) mice were used in the experiments and were obtained from Janvier (Le Genest, France). These animals were bred and maintained in pathogen-free conditions in our bespoke animal facilities at the University of Paris. All animal\ procedures were approved by both the local Committee on the Use and Care of Animals and by our Institutional Animal Care and Use Committee.

Hematologic evaluations

Orbital plexus blood was collected in EDTA tubes from anesthetized mice. Blood cell counts were determined using an automated device (MS9; Schloessing Melet, Cergy-Pontoise, France). Blood samples were also used for cytometry analysis. All mouse sera were collected and stored at 20°C before assessing the cytokine levels.

Bone marrow and spleen analysis

For BrdU analysis, the mice received an intraperitoneal injection of 0.2 ml of BrdU (0.25 mg/ml) at 16 h before sacrifice. The mice were then killed by cervical dislocation and their bones (femurs, tibias, pelvis and humerus) and spleen were harvested. The muscle and tendon tissue were removed using a scalpel and Kim wipes. BM and spleen tissues were used for cell counting and cytometry. The BM fraction was flushed out using a syringe containing 1 x PBS supplemented with 2% fetal bovine serum (FBS). The resulting cell suspensions were filtered through a 40µM cell strainer (Corning, NY) and pelleted by centrifugation. For mechanical grinding, spleens were smashed and ground between the rough sides of frosted glass slides, and the cells were then collected in DMEM containing 2% FBS. After subsequent incubation in a 24-well plate for 30min at 37°C in a humidified incubator, cell suspensions were passed through a 40µm cell strainer and re-suspended in DMEM containing 10% FBS. Suspensions were subjected to cytometry analysis after RBC lysis.

Cytometry analysis

Mouse erythrocytes were lysed using ACK lysing buffer (Lonza, Basel, Switzerland) prior to flow cytometry staining. Total BM and splenic cell populations were stained using a Zombie Viability kit for 15 min at room temperature and thereafter stained with biotinylated anti-mouse lineage cocktail antibodies for 30 min (Biolegend). After washing, the cells were stained for 30 min using the following monoclonal antibodies in the BD Horizon Brilliant staining buffer: anti-CD117/c-Kit (2B8)-BB700 and anti-CD34 (RAM34)-AF647

(BD Pharmingen); anti-Ly6a/Sca-1 (D7)-BV510; anti-CD150 (TC15-12F12.2)-PE-Cy7; anti-CD48 (HM48-1)-BV711 ; streptavidin APC-Cy7 (Biolegend).

For proliferation analysis, surface staining was performed as described above, and cell growth was analyzed using a commercially available kit in accordance with the manufacturer's instructions (BD Pharmingen BrdU Flow kits) with BrdU-AF488 (BD Biosciences, Franklin Lakes, NJ). Data acquisition and/or analysis was performed on the Cochin Cytometry and Immunobiology Facility Cytometry analyses using a Fortessa cytometer (Becton Dickinson), and Kaluza software. To assess cell viability, surface labelled cells were resuspended in AnnexinV binding buffer, and AnnexinV (FITC) was added 15 min before analysis. The cells were then evaluated using a FITC-conjugated AnnexinV labeling detection kit (BD Pharmingen). The list of antibodies used for flow cytometry is provided in the key resources table above.

Reconstitution assays

Donor cells were isolated from 6-12-week-old B6.SJL-Ptprc^{a}Pepc^{b}/BoyCrl congenic mice (*Ly5.1)* and *Ly5.2* mice at 3 days after a phenylhydrazine (PHZ) (60 mg/Kg, IP) injection or not. The hind limbs were extracted from these animals after sacrifice and cleaned. The total BM was flushed and then passed through a 40µM cell strainer to obtain a single cell suspension. A mix of cells from PHZ-treated and untreated mice was prepared in a 1:1 ratio. A mix of $5x10^{6}$ of these cells was then resuspended in a total volume of 0.2 mL and transplanted into 5 irradiated (9Gy) CD45.1 C57/BL6 recipient mice. Chimerism analysis was performed three months post-reconstitution using cytometry.

Cytokine bead array

Sera were separated from blood cells within 2 hours of blood collection by 2 successive centrifugations, and were immediately frozen at -80°C. Twenty cytokines (G-CSF (CSF-3), GM-CSF, IFNalpha, IFNgamma, IL-1alpha, IL-1beta, IL-2, IL-2R, IL-3, IL-4, IL-6, IL-10, IL-12p70, IL-13, IL-17A (CTLA-8), IP-10 (CXCL10), MCP-1(CCL2), MIP-1 alpha (CCL3), MIP-1 beta (CCL4), TNF alpha) were measured simultaneously using a multiplex magnetic Luminex Assay (ProcartaPlex TM; ThermoFisher Scientific) with the data read on a Bioplex MAGPIX Multiplex Reader (Biorad). All assays were performed in accordance with the manufacturer's instructions. Results were expressed in pg/mL and if levels were not detectable, as 50% of the lowest standard value.

METHOD DETAILS

Mathematical model

Our Mathematical model focuses on the time behaviors of the immature compartment sizes of the erythroid lineages including different regulation effects initiated by different stresses.

The model considers six hematopoietic cell types, i.e. five immature cell types, LT-HSC, ST-HSC, MPP, CMP, MEP and the mature RBC. It describes the dynamics of the compartment sizes, denoted by $(x_i(t))$, i=1,...,6. Under homeostatic conditions, the system is stable and stays at its equilibrium x_i^*, i=1,...,6. These steady-state values are biologically observable and are considered as given data in our construction (Table 2). Let us now precisely describe our model.

For any i=1,...,5, we denote by $r_i(t)$ and $d_i(t)$ respectively the net proliferation rate and the erythroid differentiation rate at time t and we denote by d_6 the death rate of the RBCs which is a fixed positive real number. We assume that, for the five immature compartments, the net proliferation and erythroid differentiation rates depend on the dynamics of different regulators modelled by the functions $u_r(t)$ and $u_d(t)$. The dynamics of these functions will depend on the state of the five immature compartments. The dynamics of the RBC will depend on a steady-state regulation through the function n(t). The compartment sizes $(x_i(t))$, i=1,...,6, satisfy the following system of ordinary differential equations:

$$\frac{dx_1}{dt}(t) = (r_1(t) - d_1(t))x_1(t) \qquad \text{(Equation 1)}$$

Where

$$r_i(t) = r_i^* \left(25\, m_r\, u_r(t)\right)^{\alpha_i};\quad d_i(t) = d_i^* \left(\frac{m_d}{25}\, u_d(t)\right)^{\beta_i}. \qquad \text{(Equation 2)}$$

The parameters r_i*, d_i* are positive numbers and the parameters α_i, β_i are non-negative numbers. The dynamics of the regulators u_r and u_d are given by the equations

$$\frac{du_r}{dt}(t) = \frac{1}{y(t)^2} - m_r u_r(t)\ ;\ \frac{du_d}{dt}(t) = y(t)^2 - m_d u_d(t). \qquad \text{(Equation 3)}$$

with y(t) the total number of cells in the five immature compartments renormalized by their size at equilibrium, m_r and m_d the positive parameters of the linear degradation terms. More precisely, we have $y(t) = \sum_{i=1}^{5} \frac{x_i(t)}{x_i*}$ with x_i* the equilibrium value of $x_i(t)$ corresponding to the cell size of type i biologically observed (Table 2).

Further, the term $2^{n(t)}$ represents the RBC produced following one MEP differentiation. We assume that the regulation of n(t) occurs (essentially through EPO) at a short time-scale and directly depends on the RBC number (Knaupp et al., 1985). Following this phenomenological approach and based on the data, we chose n(t) as a θ-logistic type function

$$n\left(t\right) = n^* + \left(33 - n^*\right)\left(1 - \left(\frac{x_6(t)}{x_6^*}\right)^c\right). \qquad \text{(Equation 4)}$$

The parameter n* is the value of n(t) at the equilibrium of the system and 33 is an upperbound of this quantity (Hayflick, 1965). The parameter c is a positive number which will be calibrated by the algorithm.

The regulation shapes have been chosen in such a way that $25 m_r u_r(t), \frac{m_d}{25} u_d(t) \frac{x_6(t)}{x_6^*}$ and are equal to 1 when the system is at its given biological equilibrium x_i*, i=1,.., 6, under homeostatic conditions.

We can prove by a straightforward computation (assuming that α1 or β1 is non zero), the uniqueness of the positive steady-state of the regulated system (1), which is also given by (x_i*), i=1,.., 6. The system is nonlinear and it is very hard to rigorously prove that it converges effectively to (x_i*), i=1,.., 6, when t tends to infinity. Nevertheless a numerical analysis based on a large number of simulations shows this convergence.

Explanation for the 6-compartments choice

In the previous section, the number of compartments has been chosen equal to 6 since we focused on the immature cell compartments LT-HSC, ST-HSC, MPP, CMP, MEP plus the RBC for which we have data.

In this paragraph (independent of the other ones), we wished to formally justify the number of 5 compartments as the minimal number of immature compartments (including MEP) explaining the following biological informations 1 to 4,

Information 1: The RBC number x_k* and the RBC death rate d_k are known, approximatively equal respectively to $5.17 * 10^{10}$ RBC per mouse and a 40-day life expectancy.

Information 2: The LT-HSC number x_1* was evaluated from the proportion of LT-HSC (Lin-Sca-1+ c-kit+, LSK CD150+ CD$48-) estimated as described in Figure S1. Knowing that a C57B16 mouse displays ≈ 250 * 106 BM cells. (Boggs, 1984; Chervenick et al., 1968; Mahajan et al., 2015), the LT-HSC number was around 15248 +/- 2200/mouse.

Information 3: By calibration τ_1=0.012 (per day), D_min=0.0845.

Information 4: The n* number of mitosis between the two last compartments was assessed as follows: we assume that the (k-1)-compartment is upstream of BFU-E (Burst-Forming-Unit Erythroid)-enriched cells known to perform ≈ 11 cell divisions *in vitro* to generate mature RBC (Li et al., 2019). Therefore, we assume that n* ≧ 10.

Let us consider a similar system as (1) but with k compartments, always assuming that the first and the last compartments correspond respectively to the LT-HSC and the RBC. Let us assume that the

system is at equilibrium. The model has been constructed so that the net proliferation and erythroid differentiation rates at equilibrium are given respectively by r_i^* and d_i^*. The net proliferation rate r_i^* is defined as $r_i^* = R_i^* - \mu_i$, R_i^* being the renewal rate in compartment i and μ_i the rate of differentiation to non-erythroid lineage. The cell death is assumed negligible (cf. Domen et al., 2000). We assume that $r_i^* > 0\$$ and $d_i^* > 0$. (cf. Busch et al., 2015).

We denote by $\tau_i = d_i^* + R_i^* + \mu_i$, the total jump rate for a type-i cell. When a jump event for such a cell occurs, with probability $p_i^d = d_i^*/\tau_i$, it is considered as differentiation event, with probability $p_i^R = R_i^*/\tau_i$, as renewal event and with probability $p_i^\mu = \mu_i / \tau_i$, as death event.

The two first compartments are the LT-HSC and ST-HSC compartments. We assume that at equilibrium, the number of LT-HSC is constant and then $r_1^* = d_1^*$. We also assume that there is a unique differentiation lineage at this step. Then, $\mu_1 = \mu_2 = 0$. In particular, $\tau_1 = 2r_1^* = 2d_1$ and $\tau_2 = d_2^* + r_2^*$.

We easily obtain that the stationary point $x^* = (x_1^*, \ldots, x_k^*)$ satisfies the following system

$$\begin{aligned} &x_1^*, \\ &x_2^* = \frac{2d_1^*}{d_2^* - r_2^*} x_1^*, \\ &x_i^* = \frac{2d_{i-1}^*}{d_i^* - r_i^*} x_{i-1}^* \ , \quad \text{for } i = 3, 4, .., k-1, \\ &x_k^* = \frac{2^{n*} d_{k-1}^*}{d_k} x_{k-1}^* . \end{aligned} \qquad \text{(Equation 5)}$$

Note that if there exists an integer i between 2 and k-1 such that $d_i^* \leqq r_i^*$, there is no stationary point such that $x_1^* > 0$ and $x_i^* \geqq 0\$$. Indeed, if $d_i^* < r_i^*$ then from (Equation 5), we obtain $x_i^* < 0$ and assuming that there exists a stationary point $x^* = (x_1^*, \ldots, x_k^*)$ such that $d_i^* = r_i^*$ then $x_i^* < \infty$ implies $x_{i-1}^* = 0$ and recursively we get $x_1^* = 0$.

From now and for any i=2, ..., k-1, we assume that $Di = (d_i^* - r_i^*)/\tau_i > 0$. Note that $Di = p_i^d + p_i^\mu - p_i^R$. The factors (Di), for $i \in \{2, \ldots, k-1\}$, play a main role in the amplification mechanism. The stationary compartment sizes can be given in an explicit form in terms of the Di and p_i^μ. Indeed, computation using that $p_i^d + p_i^\mu + p_i^R = 1$ and that $Di = p_i^d + p_i^\mu - p_i^R$, implies that

$$x_2^* = \frac{\tau_1 \tau_2}{D_2} x_1^*; \ldots; x_i^* = \frac{(1 + D_{i-1} - 2p_{i-1}^\mu) .. (1 + D_2)\tau_1}{D_i \ldots D_2} x_1^*; \ldots; x_k^* = \frac{2^{n*-1}(1 + D_{k-1} - 2p_{k-1}^\mu) .. (1 + D_2)\tau_1}{D_{k-1} \ldots D_2 d_k} x_1^* .$$

Since $p_i^\mu \geqq 0$ and $Di \geqq D\_min$, where $D\_min = \min_{\{i>1\}} Di$, it comes that

$$\frac{x_k^*}{x_1^*} \leq \frac{2^{n*-1}\tau_1}{d_k} \left(1 + \frac{1}{D\_min}\right)^{k-2}.$$

That is,

$$k \geq \frac{\log\left(\frac{d_k x_k^*}{2^{n*-1}\tau_1 x_1^*}\right)}{\log\left(1 + \frac{1}{D\_min}\right)} + 2. \qquad \text{(Equation 6)}$$

Then adding altogether Informations 1 to 4, we obtain from (Equation 6) that $k \geqq 5.32$, hence a minimal of 6 compartments (i.e. 5 immature compartments) is needed to explain the biological data.

Calibration of the parameters

Calibration of rest cell dynamics parameters. We have seen that the global system (1) admits the unique equilibrium x* and that near equilibrium, the regulation functions are all close to 1. Then if the initial conditions are close to the equilibrium x*, the dynamical system approximatively is written as

$$\frac{dx_1}{dt}(t) = (r_1* - d_1*)x_1(t)$$
$$\frac{dx_i}{dt}(t) = 2d_{i-1}* x_{i-1}(t) + (r_i* - d_i*)x_i(t); \quad \text{for i} = 2, \ldots, 5,$$
$$\frac{dx_6}{dt}(t) = 2^{n*} d_5* x_5(t) + d_6 x_6(t).$$

The aim of this section is to determine the values of the parameters (x_i*,r_i*,d_i*,n*) from the biological data of the rest cell system. Recall that r_i* is the net proliferation rate, equal to the difference between the proliferation rate R_i* and the death rate μ_i due to the differentiation of cells to non-erythroid lineages.

Let us recall that d_1*= r_1* and that the equilibrium satisfies (Equation 5) with k=6. Let us also recall that d_6=1/40 d^{-1}. In what follows, we will estimate from the biological BrdU data under homeostatic conditions and from the values of μ_i found in (Busch et al., 2015), the value of the differentiation rates d_i* and then of the proliferation rates R_i*.

Our biological data allow to estimate the values of the population sizes at equilibrium (under homeostatic conditions) (x_1*,...,x_6*), and the cell proportion that are BrdU positive after 20 hours for the 5 first types: (p_1^{BrdU},...,p_5^{BrdU}).

Let us now explain how we use these BrdU positive cell proportions, that are the proportions of cells that have made a division at least once in 20h. An estimation is given by

$$p_i^{BrdU} = \frac{x_i^D(20h)}{x_i^*}$$

with x_i^D(t) the number of cells having made a division at least once in a time interval of length t. Indeed, the type-i cell number is assumed (almost) constant equal to x_i*. The dynamics of x_i^D are then described by the following equations

$$\frac{dx_1^D}{dt}(t) = r_1^* x_1^D(t) + 2\left(r_1^* + \mu_1\right)\left(x_1^* - x_1^D(t)\right) - d_1^* x_1^D(t), \qquad \text{(Equation 7)}$$
$$\frac{dx_i^D}{dt}(t) = r_i^* x_i^D(t) + 2\left(r_i^* + \mu_i\right)\left(x_i^* - x_i^D(t)\right) + 2d_{i-1}^* x_{i-1}^* - d_i^* x_i^D(t), \quad \text{for } i \in \{2, \ldots 5\}$$

with x_i^D(0)=0. Indeed, each dividing type-i cell becomes a type-i cell that has made a division and each type-(i-1) cell differentiating in the erythroid lineage gives two cells of type i that have made a division at least once. In addition, each type-i cell that has made at least one division gives cells of type i+1 by differentiation.

By resolving (Equation 7), we obtain that

$$x_1^D(20h) = \frac{2R_1^* x_1*}{R_1^* + \mu_1 + d_1^*}\left(1 - e^{-\left(R_1^* + \mu_1 + d_1^*\right)\frac{20}{24}}\right)$$

and for i = 2,...,5,

$$x_i^D(20h) = \frac{2R_i^* x_i* + 2d_{i-1}^* x_{i-1}*}{R_i^* + \mu_i + d_i^*}\left(1 - e^{-\left(R_i^* + \mu_i + d_i^*\right)\frac{20}{24}}\right).$$

We finally deduce that

$$p_1^{BrdU} = \frac{2\left(r_1^* + \mu_1\right)}{r_1^* + 2\mu_1 + d_1^*}\left(1 - e^{-\left(r_1^* + 2\mu_1 + d_1^*\right)\frac{20}{24}}\right),$$

And then $r_1^* = d_1^* = -\frac{24}{40}\log(1 - p_1^{BrdU}) - \mu_1$.

We also obtain that for i=2,...,5,

$$p_i^{BrdU} = \frac{2\left(r_i^* + \mu_i\right)x_i* + 2d_{i-1}^* x_{i-1}*}{\left(r_i^* + 2\mu_i + d_i^*\right)x_i*}\left(1 - e^{-\left(r_i^* + 2\mu_i + d_i^*\right)\frac{20}{24}}\right)$$

But, since by (Equation 5), for i =2,...,5, $d_i^* = r_i^* + \frac{2d_{i-1}^* x_{i-1}*}{x_i*}$, we deduce that for i=2,...,5,

$$p_i^{BrdU} = 1 - e^{-\left(2r_i^* + 2\mu_i + \frac{2d_{i-1}^* x_{i-1}^*}{x_i^*}\right)\frac{20}{24}}.$$

That implies

$$r_i^* = -\frac{24}{40}\log\left(1 - p_i^{BrdU}\right) - \mu_i - \frac{d_{i-1}^* x_{i-1}*}{x_i*}.$$

These formulae allow us to compute from one to the next the values of the differentiation rates and then the net proliferation rates, using our biological data of BrdU positive proportions at equilibrium and the values μ_i given in (Busch et al., 2015).

Calibration of feedback parameters

Values of the 13 parameters associated with the regulation functions (namely c, m_r, m_d, α_i and β_i) were estimated from *in vivo* cell counts in the 6 observed cell compartments following PHZ administration (see Figure 2). Note that our model has not been designed to encompass the effect of PHZ and the corresponding loss of erythropoietic cells observed during the first three days. Then we considered only data from day 3 and later. We added two artificial data points at days 70 and 90, accounting for a return to equilibrium after two months.

Formally, parameters values have been chosen to minimize the residual sum of squares

$$RSS = \sum_{i,j}\left(\frac{x_i\left(t_j^i\right)^2 - X\left(t_j^i\right)}{x_i\left(t_j^i\right)}\right) \qquad \text{(Equation 8)}$$

where x_i and X_i denote respectively the *in silico* and *in vivo* cell numbers in compartment i and t^i_j are the days when the cell numbers in the i-th compartment has been measured.

Hence, the initial conditions at day 3 have been chosen as

$$x_1(3) = 0.006\left(\times 10^6 \text{ cells/mouse}\right) \quad x_2(3) = 0.0152\left(\times 10^6 \text{ cells/mouse}\right) \quad x_3(3) = 0.02\left(\times 10^6 \text{ cells/mouse}\right)$$

$$x_4(3) = 0.093\left(\times 10^6 \text{ cells/mouse}\right) \quad x_5(3) = 0.395\left(\times 10^6 \text{ cells/mouse}\right) \quad x_6(3) = 0.94\left(\times 10^6 \text{ cells/mouse}\right)$$

$$u_r(3) = \frac{1}{m_r y(3)^2} \qquad u_d(3) = \frac{y(3)^2}{m_d}$$

Minimization has been achieved with the Covariance Matrix Adaptation in Evolution Strategy (CMA-ES) from Python package cma. Optimal parameters obtained by this method are presented in Table 3 and the corresponding cell dynamics in Figure 2.

While we did not formally prove the existence of a unique optimal set of parameters, the same set, within 10^{-3}, has been obtained with ten independent runs of the stochastic CMA-ES algorithm, implying numerical identifiability.

The identifiability of the system (1), (Equation 2), (Equation 3), and (Equation 4) has been assessed on synthetic data produced from random set of parameters. The model was efficient to retrieve the parameter set behind the synthetic data.

Sensitivity analysis

The sensitivity of the cost function RSS (Equation 8) to the parameters estimated in the previous subsection has been assessed by plotting its values with respect to variation of each parameter.

We also deduced from this figure that the variation of each parameter in the following intervals induces a maximal variation of 15% of the cost function RSS above its minimal value:

$$\begin{cases} m_r \in [0.0948,\ 0.109] \\ m_d \in [0.0475,\ 0.068] \\ \alpha_1 \in [4.42,\ 4.69] \\ \alpha_2 \in [4.24,\ 4.76] \\ \alpha_3 \in [3.9,\ 4.07] \\ \alpha_4 \in [1.9,\ 2.45] \\ \beta_1 \in [8.84,\ 9.45] \\ \beta_2 \in [8.3,\ 9.6] \\ \beta_3 \in [7.81,\ 8.69] \\ \beta_4 \in [5.58,\ 6.9] \\ \beta_5 \in [4.15,\ 5.62] \end{cases}$$

Note that parameter c (Equation 4) only affects the number of RBCs and weakly influences the value of the cost function RSS. Then this parameter is poorly indicative but remains numerically identifiable (as seen in the previous section).

QUANTIFICATION AND STATISTICAL ANALYSIS

The data shown in all of the figures are the mean values+/- SD. Statistical details relevant to each experiment including the sample numbers and experimental repeats are listed in the Figure legends. Data were statistically analyzed using the Mann-Whitney test.